Journal of Materials and Electronic Devices 1 (2023) 18-32

Scanning Tunnelling Microscopy: Beyond Imaging Surfaces, Atoms and Molecules

Doğan KAYA[1*]

[1*]Department of Physics, Faculty of Science and Literature, Cukurova University, 01160 Cukurova, Adana, TURKEY

Direct observations of surfaces, individual atoms and molecules have been achieved after the invention of Scanning Tunneling Microscopy (STM). The STM, which was invented by Binnig and Rohrer in 1981, has become an indispensable tool and it has revolutionized the real-space imaging of molecules, providing a detailed understanding (growth, nucleation, electronic coupling to the surface) and how they interact with each other and with surface atoms. Here, STM can be used as a powerful tool not only imaging but also manipulating individual atoms/molecules to obtain desired geometries for nanoscale applications. Such as mechanical (lateral, vertical), electric field-induced, and elastic-inelastic tunneling-induced manipulation are all major techniques that can be applied via STM. In this chapter, the mechanism, techniques and capabilities of the STM will be introduced.

Keywords: *STM; Probe Microscopy; Imaging*
Submission Date: 24 December 2022
Acceptance Date: 18 February 2023

**Corresponding author: dogankaya@cu.edu.tr*

1. Introduction

1.1. Probe Microscopy Types

Producing an image of an atom was a great interest and challenge for scientists in the last century. After the invention of the transmission electron microscope (TEM) and the scanning electron microscopy (SEM) [1, 2] we could obtain more information about atoms and surfaces via high-resolution atomic images. The scanning tunneling microscope (STM) was later invented in the IBM laboratory in Zurich by Binnig and Rohrer in 1981 and they received the Nobel prize in Physics 1986 for their outstanding contribution to science [3]. When the metallic STM tip is located over a conducting surface above 0.5-1 nm and a voltage applied between the tip and the substrate, the electrons can tunnel in the vacuum gap and reach the surface to provide a topographic image of the surface via scanning the surface in x and y directions. The tip-surface distance can be precisely controlled by the tunneling current and so the high-resolution images of surfaces, atoms or molecules can be obtained. This is possible with moving the tip in an x, y and z directions via the sub-nanometer level mechanical extension of piezoelectric actuator elements. During scanning the surface at constant current mode (or constant height mode), a feedback loop mechanism constantly adjusts the tip height (or tunneling current) which provides the topography of the surface.

The STM works based on a quantum tunneling mechanism and capable of not only imaging single atoms but also manipulate single atom/molecule on surfaces. The first study of atomic manipulation was displacing xenon (Xe) atoms on nickel (Ni) surface at 4 K [4]. They could displace Xe atoms on the surface and decorate the IBM initials using the tip of the STM. Now, the STM has been extensively used to create high-resolution images of surfaces, individual atoms/molecules for nanotechnology applications. There are various manipulation mechanisms: such as mechanical (lateral, vertical) [5-13], electric-field induced [14-18], and elastic/inelastic tunneling induced techniques [19-21]. These

techniques of STM have been widely investigated not only to determine the physical, chemical, electronic, and bonding properties of adsorbed atoms/molecules and nanostructures but also obtain desired geometries and structures at the nanoscale [22-26].

One of the greatest challenges for researchers is building things small, effective and with desired properties at nanoscale and realistic temperatures for technological applications [27]. Therefore, self-assemblies [28-31], supramolecules [32-34], two- or three-dimension materials on surfaces are considerable interest due to their diverse potential applications in e.g. solar cells, catalysis, organic electronics and single-molecule devices for nanoelectronics [35, 36]. The STM is a versatile tool to reveal all properties of these adsorbents and nanostructures via imaging and spectroscopic techniques. Moreover, the manipulation of selected atoms, molecules, and nanostructures on different surfaces are possible to obtain unique outcomes using different STM approaches [7, 13, 37-42].

1.2. The Concept of Tunneling Mechanism

Before discussing the STM-based experiments it is worthwhile to first briefly recap the working principles of the STM. If a particle does not have sufficient energy (E<V) to cross a potential barrier with a height of U_0 and width of L, it will never pass through the barrier by the law of classical mechanics. On the contrary in quantum mechanics, when a particle with an energy of E meets for the same potential barrier, there is a finite probability of the particle traversing the classically forbidden region and being found on the other side. This phenomenon is known as *tunneling* and can be explained by solving the Schrödinger equation.

The one-dimensional rectangular potential barrier showed in **Hata! Başvuru kaynağı bulunamadı.**(a) with a height of U = U_0 potential in the region of 0 ≤ x ≤ L [25]. The solution of the wave function for the three regions and the transmission coefficient can be found via the Schrödinger equation, as shown below,

$$-\frac{\hbar^2}{2m}\frac{d^2}{dx^2}\Psi(x) + U\Psi(x) = E\Psi(x).$$

Where $\hbar$ is Planck's constant, m and E are the mass and the energy of the particle, respectively. We can consider three regions, I, II, and III, as seen in **Hata! Başvuru kaynağı bulunamadı.**(a) and the solution of the wave functions, $\Psi_n(x)$, will be different in each region which can be given as,

x ≤ 0 and U = 0

$$\Psi_1(x) = Ae^{+ik_1x} + Be^{-ik_1x},$$

$$k_1 = \frac{\sqrt{2mE}}{\hbar},$$

0 ≤ x ≤ L and U = U_0

$$\Psi_2(x) = Ce^{+k_2x} + De^{-k_2x},$$

$$k_2 = \frac{\sqrt{2m(U_0-E)}}{\hbar},$$

L ≤ x and U = 0

$$\Psi_3(x) = Fe^{+ik_1x} + Ge^{-ik_1x},$$

$$k_1 = \frac{\sqrt{2mE}}{\hbar}.$$

In the first region, the wave function of $\Psi_1(x)$ has two coefficients A and B, transmitted and reflected, respectively. In the second region, the second term of *D* becomes zero and the function exponentially decays. The coefficients of these equations (A, B, C, D, F, and G) can be found in terms of the decay constants k_1, k_2 and k_3 by inserting the boundary conditions into the wave functions at x = 0 and x = L. The functions at x = 0 and x = L are also differentiable and continuous. In the region three, the particle only transmitted and there is no reflection. Therefore, G becomes zero and the probability of a particle being transmitted in the region three is given by,

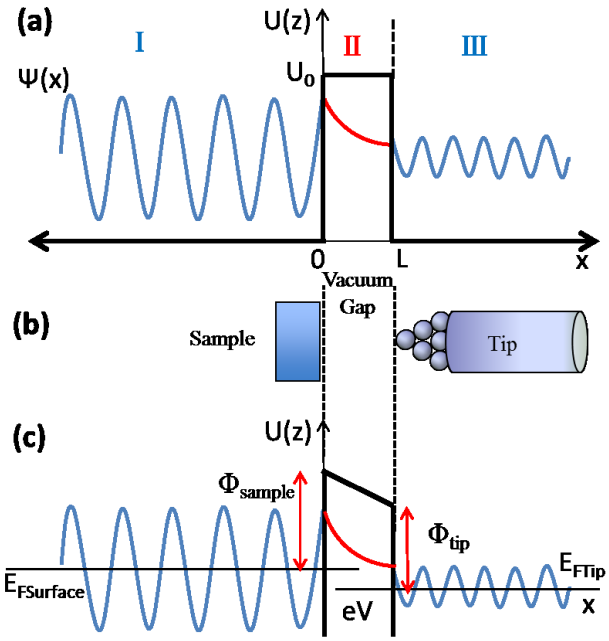

Figure 1: (a) The schematic diagram for a one-dimensional potential barrier with U=U_0 in the range of 0 ≤ x ≤ L shows quantum tunneling. (b) Sample-tip positions in the vacuum gap. (c) A one-dimensional potential barrier diagram representative of tunneling in the STM. L is the tip-sample separation distance; the work function of the sample (tip) is Φ_{sample} (Φ_{tip}). Here a positive voltage is applied to the tip which means the electron tunnels from the sample surface to the tip through the vacuum.

$$T = \frac{|\Psi_3(transmitted)|^2}{|\Psi_1(\text{incident})|^2} = \frac{F*F}{A*A}.$$

After finding the coefficients and using the fact that $k_2L \gg 1$, the transmission probability becomes,

$$T = \frac{16E}{U_0}\left(1 - \frac{E}{U_0}\right)e^{-2k_2L} \cong e^{-2k_2L}.$$

Therefore, the transmission probability of particle decays exponentially throughout region 2 [25].

In the tunneling regime, the tip-sample distance is about 5-15 Å, the number of electrons tunnel through the vacuum energy barrier in the presence of bias voltage [43, 44]. The bias voltage, tip or sample, causes a shift of the Fermi energy level away from equilibrium. This shift represented in **Hata! Başvuru kaynağı bulunamadı.**(c) with a one-dimensional potential barrier diagram. Here, L is the tip-sample separation distance and the work function of the sample (tip) is Φ_{sample} (Φ_{tip}). The shaded areas show the occupied states for the surface, $E_{Fsurface}$, and the tip, E_{Ftip}-eV. As shown in **Hata! Başvuru kaynağı bulunamadı.**(c), the filled sample states are shifted by eV from the Fermi energy level of the tip. Therefore, there is a probability that the electrons can tunnel from $E_{Fsurface}$ to unoccupied tip states. When a positive bias voltage is applied to the tip, the average work function can be written as,

$$\Phi = \frac{1}{2}(\Phi_{\text{samp}} - \Phi_{\text{tip}}).$$

And the decay constant becomes

$$k = \frac{\sqrt{2m(\Phi - E)}}{\hbar}.$$

Applying a bias voltage increases the Fermi energy of the surface, thus, the electrons (0 < E < eV) can tunnel through the tip to fill empty states in the tip state. The transmission probability for a small bias voltage, $\Phi \gg$ eV, is:

$$T(x = L) = e^{-2\frac{\sqrt{2m\Phi}}{\hbar}L}.$$

When a large bias voltage applied to the tip, the energy, E, is included so the transmission probability is given by:

$$T(x = L) = e^{-2\frac{\sqrt{2m(\Phi - E + eV/2)}}{\hbar}L}.$$

There is a probability that electrons tunnel the barrier, thus, the tunneling current can be written as,

$$I \propto \sum_{E_n = E_F - eV}^{E_F} |\Psi(\mathrm{x})|^2 \, e^{-2kL}.$$

The local density of state (LDOS) [25], which is related to the Fermi energy of the sample, is given by

$$\rho(x, E) \propto \frac{1}{eV} \sum_{E_n = E_F - eV}^{E_F} |\Psi(\mathrm{x})|^2.$$

Finally, the tunnelling current can be expressed as

$$I \propto \int_0^{eV} \rho(0, E) T(x, E) dE,$$

$$I \propto \mathrm{V}\rho(0, E_{Fsample}) e^{-1.025\mathrm{L}\sqrt{\Phi}}.$$

The tunneling current is proportional to the local density of surface states and the applied bias voltage. The current shows an exponential dependence in the region of the tip-sample separation, L. For example, decreasing the tip-sample separation by 1 Å causes the tunnel current to increase by a factor of ten [25]. Therefore, the tunneling current can be extremely sensitive to atomic-scale corrugations on a sample surface to obtain atomic-resolution images.

Finally, an important capability of the STM is Scanning Tunnelling Spectroscopy (STS) which allows us to measure the occupied and unoccupied local density of states (DOS) of the atoms/molecules and nanostructures on the surfaces. Measuring a current-to-voltage characteristic of the tunneling junction at a constant tip-sample distance by sweeping the voltage (typically from -2.0 V to +2.0 V) and recording the tunneling current provides energy-resolved spectroscopic data with an atomic resolution. The differentiation of the I-V curve gives the LDOS [25] which depends on the tunneling gap (d), Fermi energy of sample ($E_{Fsample}$), transmission factor for tunneling (T) and ρ_{tip}. However, due to the uncertainty of the tip density of state, ρ_{tip} is usually considered as constant,

$$\frac{dI}{dV} \propto \frac{4\pi e^2}{\hbar}\rho_{tip}(0)\rho_{sample}(eV)T(eV, V, d).$$

So, the derivative can be simplified as

$$\frac{dI}{dV} \propto \rho_{sample}(eV).$$

1.3. 1.3. Scanning Tunneling Microscopy Design

The fundamental physics behind the STM is the quantum tunneling effect, which occurs when a bias voltage is applied between a sharp metallic probe (the STM tip) and a surface that are less than 1.5 nm apart [3, 44]. Once the tunneling current is detected the surface topography can be imaged by rastering the tip in the x and y directions. During a surface scan, a small change in the distance between the tip and the surface can be determined by observing the change of the tunneling current. Thus, a surface image can be generated by recording tip displacement due to the tunneling current over the surface. Besides an atomic-resolution image is strongly dependent on the sharpness of the tip and the local density of the state of the sample [36, 45]. **Hata! Başvuru kaynağı bulunamadı.**(a) shows a schematic diagram that illustrates the essential components of an STM system.

The electronics in the STM plays a crucial role for fine tip control and data acquisition. It consists of four major units. First of all, a high-voltage amplifier for piezo tube motion in x, y, and z directions. Nowadays the tube [46] or the beetle type [47] scanners are most in use for STM design. These designs contain, first, coarse approach systems to expeditiously bring the tip the closest distance to the surface. Following the piezo actuator elements reduce the distance up to 5-15 Å and the tip scans the surface with a range of several micrometers with a fine motion (0.01 nm/step). These motions can be controlled in angstrom level in x, y, and z directions by voltage pulses on piezo actuators and tunneling current. Second, the current amplifier controls the tunneling current in a range of 0.01-10 nA in the tip/sample gap, so the

tip motion. In the tunneling regime, the wavefunctions of tip and sample overlap and the tunneling conductance are detected so that the scanning process can be started. Therefore, the current amplifier is the indispensable element of an STM for atomic-resolution data acquisition. Third, a digital feedback controller: the current amplifier converts the tunneling current to a voltage by controlling and compare applied bias voltage and tunneling current between sample and tip. When the absolute value of the current is negative, the z-piezo withdraws by the feedback controller to adjust the position. Thus the surface topography can be obtained via controlling tip motion in z-direction. Finally, a data processing and control unit operates all electronics and data acquisition processes. At constant tunneling current, a feedback system is required for control of the z-height displacement of the tip. The STM can work in different modes: a constant current mode (**Hata! Başvuru kaynağı bulunamadı.**(b)) and a constant height mode (**Hata! Başvuru kaynağı bulunamadı.**(c)). For the constant current mode, during scanning, the tunneling current and bias voltage are fixed, as the tip scans the surface and the z-height constantly adjusted via a feedback loop to maintain a constant current. Therefore, the z trajectory represents the surface topography via a constant charge density of the surface. The contrast on the image is due to variations in charge density [48]. On the other hand, in constant height mode, the z-position of the tip is fixed and the tunneling current change depending on variations in the tip-sample separation due to the surface topography.

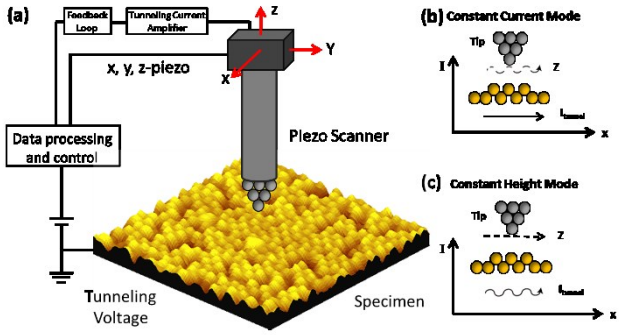

Figure 2: (a) Schematic illustration of the components of an STM system, such as tip, x, y, and z-piezo, feedback loop electronics, tunneling current amplifier, and data processing and control unit. Two different scanning modes are presented: the constant current mode, (b) or constant height mode, (c). The surface topography can be recorded using x, y, and z-piezo which is controlled by a feedback loop to control the tip displacement.

The electronics in the STM plays a crucial role for fine tip control and data acquisition. It consists of four major units. First of all, a high-voltage amplifier for piezo tube motion in x, y, and z directions. Nowadays the tube [46] or the beetle type [47] scanners are most in use for STM design. These designs contain, first, coarse approach systems to expeditiously bring the tip the closest distance to the surface. Following the piezo actuator elements reduce the distance up to 5-15 Å and the tip scans the surface with a range of several micrometers with a fine motion (0.01 nm/step). These motions can be controlled in angstrom level in x, y, and z directions by voltage pulses on piezo actuators and tunneling current. Second, the current amplifier controls the tunneling current in a range of 0.01-10 nA in the tip/sample gap, so the tip motion. In the tunneling regime, the wavefunctions of tip and sample overlap and the tunneling conductance are detected so that the scanning process can be started. Therefore, the current amplifier is the indispensable element of an STM for atomic-resolution data acquisition. Third, a digital feedback controller: the current amplifier converts the tunneling current to a voltage by controlling and compare applied bias voltage and tunneling current between sample and tip. When the absolute value of the current is negative, the z-piezo withdraws by the feedback controller to adjust the position. Thus, the surface topography can be obtained via controlling tip motion in z-direction. Finally, a data processing and control unit operates all electronics and data acquisition processes. At constant tunneling current, a feedback system is required for control of the z-height displacement of the tip. The STM can work in different modes: a constant current mode (**Hata! Başvuru kaynağı bulunamadı.**(b)) and a constant height mode (**Hata! Başvuru kaynağı bulunamadı.**(c)). For the constant current mode, during scanning, the tunneling current and bias voltage are fixed, as the tip scans the surface and the z-height constantly adjusted via a feedback loop to maintain a constant current. Therefore, the z trajectory represents the surface topography via a constant charge density of the surface. The contrast on the image is due to variations in charge density [48]. On the other hand, in constant height mode, the z-position of the tip is fixed and the tunneling current change depending on variations in the tip-sample separation due to the surface topography.

2. STM Instrumentation

2.1. Piezo Electrics

The principles of STM are not complicated but the operating systems are important to produce reliable results. These systems control the tip movement with piezoelectric actuators at the angstrom level and reduce electronic noise, thermal drift, creep and vibration. To move the STM tip in x, y and z-direction first a coarse approach takes place with computer programed step-motors. Then the tube piezoelectric elements, which are discovered by the Curie brothers in 1880 [49, 50], are used as an actuator to scan sub-angstrom (~0.1 Å) level. Applying a voltage to outer the

electrodes results in an extension due to the electric field created in the piezo. Non-centrosymmetric crystals [51] and $Pb[Zr_xTi_{1-x}]O_3$ [52] are mostly used as the piezoelectric actuators. For the application of the piezoelectric actuators in the STM, the piezoelectric coefficient should be about Å/V level for the preferred materials. These materials mostly ferromagnetic and above the Curie temperature (for PTZ is about 673 K [52]) transforms anisotropic structure to cubic and loses its piezoelectric properties. Therefore, in the STM, the experiments (depends on design) and the UHV system baking process must be conducted below the Curie temperature to protect piezoelectric properties. The tube scanner design is the most widely used as an actuator for the STM scanner due to high piezo constants and high resonance frequencies. As seen in **Hata! Başvuru kaynağı bulunamadı.**(a), a schematic tube piezoelectrics design presented with assembling inner and outer metallic electrodes on which four piezo elements placed for x and y directions. With this design, the STM tip can scan a circular area in x and y directions and applied positive or negative voltages extend the piezo in both (+) and (-) directions, so the surface topographic image can be obtained.

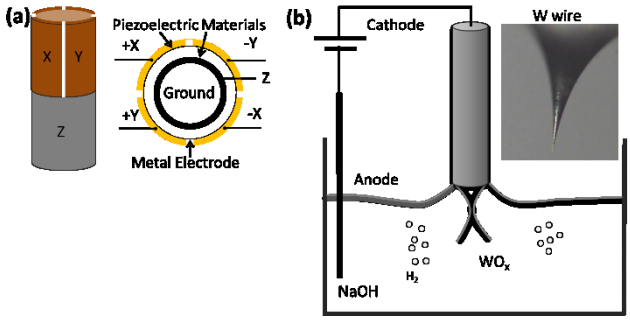

Figure 3: (a) A schematic diagram of the x, y and z-direction piezoelectric tubes with a top and side view. (b) The electrochemical tip etching demonstration. Here, the metallic tip wire is the cathode and a wire introduce in the NaOH solution serves as the anode. When voltage is applied reaction starts, the tip is etched like meniscus shape and liberates H_2 gas. An optical image (20X) of a W etched tip taken by the author.

In most of the STM scanner design, X, Y, and Z piezo scanners are not isolated from each other. Therefore the extension in x or y-directions may result in an extension in vertical (z) direction. This is because moving the STM tip a different area during scanning or sudden temperature difference on the surface and the tip. These changes may cause a large extent in the piezo actuators and so a drift can be observed as a function of time in the next image due to piezo creep. The annealing or cooling sample also results in a drift and requires a while scanning to reduce thermal drifts.

2.2. Tip Preparation

The sharpness of the STM tip can increase the probability of obtaining high-resolution images; therefore the tip preparation is one of a key aspect of the STM experiments. There are two common methods: mechanical cutting and electrochemical etching. Mechanical cutting is typically done by cutting and simultaneously pulling up on a soft wire (mostly oxidation-free Au or Ir/Pt metal tips) [53, 54] with a clipper by a given angle of the wire. Mechanical cutting usually used for ambient conditions experiments. On the other hand, electrochemical etching methods provide more control in obtaining a sharp tip when compared with mechanical cutting. The most common method is the DC drop-off method [55] for hard metal tips such as W (see **Hata! Başvuru kaynağı bulunamadı.**(b)). Before starting the etching process, the wire should be cleaned with isopropanol and acetone in an ultrasonic bath (each for 10 minutes) to remove organic contaminations. Moreover, the etching apparatus should also be clean, and the system should be isolated from any vibration to prevent a nonuniform tip forming. Placing the tip in a NaOH (KOH, HF/HNO_3, etc.) solution and applying DC voltage starts the etching process near the solution surface with creating taper formation. Continuing etching via OH^- ions, liberates H_2 gas and WO_x layer occur on the tip surface. Finally, the wire in the solution drops when the neck is thin enough and creates the like-meniscus formation. The overall electrochemical reaction between the anode and cathode is given by

$$W(s) + 2OH^- + 2H_2O \rightarrow WO^{2-}_4 + 3H_2(g).$$

Earlier works suggest that the aspect ratio of a tip should be less than 1 because a long tip (h/d>>1) causes more vibration [55, 56]. To obtain a good tip, a two-steps etching process may require to increase the probability of atomic-resolution images via providing single-sharp tips. This is because the mechanical cut may cause splitting and create a crack on the wire and these create multiple tips after the etching.

We can estimate the sharpness of the tip either the single/double/multiple tips by examining the STM images after scanning the surface. Once the tip inserted into the vacuum and before scanning a sample, a tip cleaning process must be applied. There are several methods to obtain a sharp tip. *Heat treatment*: the residual oxide layer and contaminations on the tip can be removed in-vacuum via resistive heating [56-60]. Applying direct current, so increasing the temperature over 1000 K (below-melting temperature), for several seconds allows removing the oxide layer while keeping the pressure less than 10^{-7} torr. To prevent the tip from melting, the temperature of the heat treatment and direct current methods should not exceed the melting point of the tip. *Sputtering*: the tip can be bombardment with the inert gas (Ar) ion gun at ~1 KeV to remove the oxide layer and contaminations. There are several other methods for tip sharpening during scanning. *Applying high voltage*: leaving the tip to scan at a high

voltage for several seconds creates a non-uniform electric field which results in dropping impurities and removing the residual oxide layer from the tip. *Intentional Crash*: moving the tip into the soft surfaces, such as Au(111), may results in a formation of a nanotip by picking-up surface atoms and covering the W tip apex. However, this process is not suitable for hard surfaces such as Si or HOPG surfaces that can destroy the tip apex.

2.3. Vacuum

To study surface science with the STM, the ultra-high vacuum (UHV) conditions are needed to eliminate surface contaminations and background gasses. The physics behind UHV conditions (i.e. a base pressure lower than 10^{-9} mbar) is based upon the gas density, the mean-free-path of a gas molecule ($\lambda = \frac{k_B T}{\sqrt{2}\pi\epsilon^2\rho}$), and surface contamination (Hertz-Knudsen equation $R = \frac{P}{\sqrt{2\pi m k_B T}}$) [61]. From atmospheric pressure to UHV pressure at 300 K, the gas density decreases, the mean-free-path of a gas molecule increases, and the rate of surface contamination decreases by a factor of 10^{13} [62]. Best conditions are achieved by minimizing such factors, reducing background gases and reducing contamination on the chamber walls and sample. The UHV chambers are made of materials such as glass, stainless steel, aluminum or titanium because of their low outgassing properties. To seal each connection, soft copper gaskets are widely used, which are compressed between two knife-edges flanges that are machined into the port flanges. The alternative is to use rubber gaskets. Important considerations when dealing with the UHV are pumping size, chamber conductance, and choice of low vapor pressure materials and the elimination of contaminants.

Under typical operation conditions, the UHV system needs to be pumped down to 10^{-9} mbar or lower to perform most experiments. Several types of pumps and gauges can be used to reach and measure desired pressure, respectively [63]. Here, a rotary pump is a mechanical pump and use for rough pumping to reach from atmosphere to10^{-3}mbar. Turbomolecular pump is also a mechanical pump and the operating pressure is 10^{-3}-10^{-9} mbar. The ion pump is a getter type of pump and works by applying a high voltage (typically at 3-7 kV range) to electrodes to create ions in the vacuum. These ions ionize molecules and then capture them by cathode so reaching 10^{-7}-10^{-12} mbar pressure. A titanium sublimation pump (TSP) is also a getter type of pump and usually accompanies the ion pumps to reduce H_2, CO and O_2 gases in the system. The TSP usually runs at a vacuum lower than 10^{-7} mbar by applying around 40 A direct current through a titanium wire. The sublimated Ti atoms are chemically gettering with the reactive gas molecules in the system and reduce the pressure. Generally, the type of gauge is determined by the pressure range to be measured (which is dictated by the pump used) and sometimes by the gas being pumped, e.g. whether it is corrosive. Rotary, turbomolecular, and ion (TSP) pumps are uses pirani, penning, and ionisation gauges, respectively. The venting process may require loading a sample/tip into the vacuum or to fix-or-change part of the vacuum system. This process is usually performed with pure N_2 gas, which produced from liquid nitrogen (L-N_2) or compressed N_2 gas, to reduce water vapor on the inside of the chamber walls. If the system pressure is not sufficient, the entire system should be heated to maximum temperature (usually up to 150 °C) to evaporate water vapour and other residual contaminations to pump-out from the system. An important point is the depolarization temperature of piezoelectric tubes is about 180 °C on the STM head, therefore, the baking process should not exceed this temperature. The bake-out temperature (usually up to 150 °C) is safe below the critical temperature for piezoelectric tubes and decomposition of rubber gaskets, glass windows, and vitons. Baking time varies from 24 hours to 52 hours with the system protected by an interlock against excessive pressure or temperature during baking.

2.4. Vibration Isolation

Atomic resolution data acquisition of STM requires vibration isolation systems that reduce the external perturbations and provide stability in the tunneling junction. The vibration can be transmitted through connections and can affect the tip movement in the tunneling regime which can reduce the data quality. For the STM systems, there are mainly two types of vibrations which are the continuing vibrations due to mechanical pumps and instant shocks for a short period of time. The typical vibration frequencies of a laboratory environment, motors-transformers, building, and people walking by are between 10-100 Hz, 6-65 Hz, 15-25 Hz, and 1-3 Hz, respectively. Therefore, all possible vibrations reasons should be considered for atomic resolution data acquisition in the STM.

There are two kinds of damping mechanisms: passive and active. The passive damping is based on reducing motions and the active damping system is creating an opposite motion to stop vibrations in the STM system. All STM system usually builds on pneumatic legs to diminish the typical external vibrations. To poise the STM stage in the UHV chamber, metal springs (3 or 4) usually take place resulting in low resonance frequencies (5 Hz). Viton is usually used as a spacer between metal plates and connections which create a vibration frequency of 10 to 100 Hz. Viton is a chemically stable elastomer with low outgassing rates (2.7 x 10^{-7} W/m^2[64]) material which is comparable with the UHV conditions. Cryogenic and elevated temperature STM experiments encounter vibrations

due to temperature fluctuation between STM parts. For these kinds of vibrations, magnetic eddy-current damping system is used that is a non-contact and vacuum compatibility system with a high damping capability. This system consists of copper elements and permanent magnets. Once the copper elements move between the magnets due to external perturbations, a magnetic field created in the opposite direction to reduce the motion [64].

3. High-Resolution Studies of STM

3.1. Imaging Surfaces

In the beginning, the scanning tunneling microscopy is used in surface science to conduct the surface topography of metals and semiconductors due to their interesting nature and practical applications. Some of these surfaces can be contaminated easily in air, therefore, the STM allows preparing clean surfaces in Ultra-High-Vacuum (UHV) conditions to provide atomic-resolution images and surface state properties. The heat treatment controls the surface reconstructs and electronic properties via minimizing the surface energy so strain. To explore the surface state properties, atomic diffusion, reconstructions, crystal shapes, step edges formations or grain boundaries of surfaces, the STM is the most accurate tool via its dynamic atomic resolution imaging capabilities. Reconstruction patterns, transitions, and disorder lines of surfaces can also be revealed by the STM with a high resolution and instantaneous images. But it is highly difficult so require perfect conditions such as tip, vacuum, vibrations-free environment, and cryogenic temperature.

The study of adsorbate, two and three-dimensional nanostructure formations, and surface catalysis properties are mostly performed on metal surfaces. The STM can reveal the topographic map of clean metal surfaces via obtaining the total electronic-charge density of the surface. Imaging surface properties, such as dislocations, grain boundaries, step edge diffusions of metal surfaces, are possible with the STM. The dislocations and grain boundaries modify surface stress during the crystal growth process. Moreover, the crystal growth also depends on the self or temperature triggered step edges diffusion. The STM can image these growth mechanisms via real-time imaging capability. It is easy to observe the surface directions of metal surfaces such as (111), (110) or (100) direction of Ag, Au, Cu, Mo, Pt, Pd, Ir, Cr or W surfaces [65]. Metallic surface preparation in UHV conditions provides a variety of surface reconstruction patterns, such as (1x2), (1x3), (1x4), (3x4), (7x7) [65]. The atomic resolution of metal surfaces is difficult to obtain due to free valance electrons of metals. Only a few studies could achieve an atomic resolution of surfaces in the STM, such as Au(111) [66, 67]. The roughness and phase transition of metal surfaces can be studied via STM, such as Au, Pt, and Ir, as a function of temperature.

To study the reaction of small or large molecules for surface science applications, chemically inert surfaces offer the possibility to determine adsorbate properties. One of the most preferred metal surfaces for experimental studies is the Au(111) surface due to unique surface reconstruction and easy to obtain a clean large flat surface. As seen in Figure 4(a), the reconstructed Au(111) surface exhibits clear zigzag patterns at room temperature a bias voltage of -1.8 V, called herringbone structure [66]. This reconstruction is formed of face-centered cubic (FCC) and hexagonal close-packed (HCP) stacking regions with bulged and pinched elbow sites [68, 69]. The adsorption, nucleation, growth, and formation of atoms/molecules are preferable starts from these bulged and pinched elbow sites. This allows us to determine the physical and chemical properties of adsorbents on the (111) surface. A single-atom vacancy on the elbow site occurs due to atomic distortion and plays an important role in the molecular adsorption and nucleation. The FCC region is ~3.5 nm wide and the HCP region is ~2.4 nm which are confirmed by the STM image [70]. Therefore, when atoms and molecules are deposited onto the (111) surface, there is a tendency for them to accumulate in the FCC region.

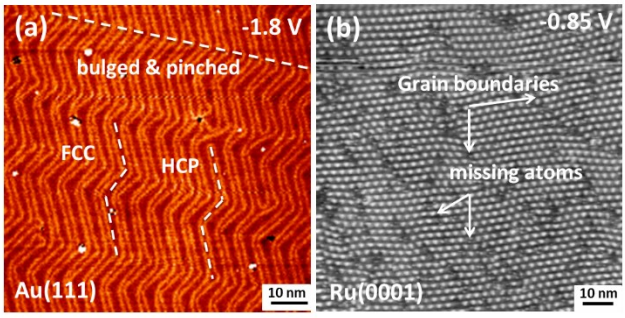

Figure 4: (a) The reconstructed Au(111) surface recorded at -1.8 V and clear zigzag patterns show FCC and HCP regions with bulged and pinched elbow sites (the image is captured by the Author). (b) Ru(0001) on graphene surface recorded at -0.85 V and missing atoms and grain boundaries indicated with white arrows [71].

To produce uniform distributed molecules or nanostructures and determine their properties, identical large flat areas require which should be easy to prepare and tolerate high temperatures. Graphene provides large flat surfaces that make a good candidate as a template and stable ambient conditions for engineering applications [71]. Figure 4(b) shows the STM image of Ru(0001) on the graphene surface, recorded at -0.85 V, single Ru atoms, missing atoms, and grain boundaries are determined at room temperature. Temperature-dependent STM study showed that Ru(0001) is uniformly formed on graphene and staple at high

temperatures which allows us to use as a template for nanostructure growths and practical applications.

The spatial resolution of semiconductor surfaces can be resolved using STMs' atomic level imaging capability. While the physical and morphological properties of semiconductor surfaces can be imaged, the local density of state can also be determined via current-voltage spectroscopy (STS). So the information of electronic structure, morphology, dangling bonds, grain boundaries, and surface defects of these surfaces can be obtained with the STM high-resolution image and spectroscopy techniques. To study optoelectronic properties of semiconductor surfaces, electron injection via the STM tip provides interesting information about electroluminescence properties. Imaging a single atom of semiconductor surfaces is easy with the STM because it does not require a conduction surface. Silicon surfaces are widely used in the semiconductor technology due to their excellent electronic properties, the ability to obtain extremely high purity Si, the abundance of the raw material, and the maturity of Si wafer processing technology [72]. As seen in Figure 5(a), the unique clean Si(111)-7x7 surface image is obtained at room temperature after annealing and reconstruction process at 1150 K in the STM. The surface imaged recorded at a bias voltage of +1.0 V and the electronic structures and the unit cell of the surface determined by scanning at high or negative voltages. The STM can only image the adatoms of the 7x7 surface because they are in the uppermost layer.

After the discovery of graphene by Geim and Novoselov [73] in 2004, it has become one of the most studied materials due to its unique electronic properties for optoelectronic devices, transistors, transparent screen technologies, and so forth [74]. As a two-dimension insulator material, graphene, that provides high intrinsic strength, electronic and heat conduction properties with a very simple preparation method. Its surface properties can only be determined by angular-resolved photoelectron spectroscopy (ARPES), scanning tunneling microscopy, or spectroscopy techniques. Figure 5(b) shows a cleaved HOPG surface image which is recorded at a bias voltage of -0.17 V. The image is presented after using the fast Fourier transform (FFT). A clear MORIÉ pattern that shows the line depicts the tilting angle of θ=30° between carbon atomic lattice (dash line) and superlattice (solid line). The topmost layer of the surface can form a mound formation due to the proximity of the metallic tip to the surface. This is because of a weak interaction between graphene layers. Therefore, preferring a low bias voltage during scanning reduces the electric field on the surface created by the tip. Moreover, the low bias (< 1 V) and high tunneling current (> 1 nA) prevents the tip/sample contact which is an undesirable situation to obtain high-resolution images and protection the tip from the potential crush.

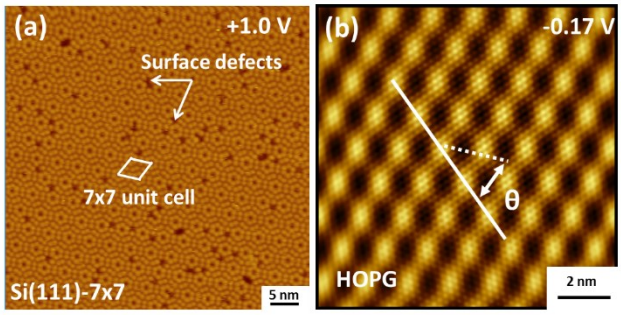

Figure 5: (a) The STM image of the reconstructed p-type Si(111)-7x7 surface recorded at +1.0 V. The 7x7 unit cell and the surface defects indicated with white diamond and arrows, respectively. (b) Cleaved HOPG surface recorded at -0.17 V and a clear MORIÉ pattern presented with carbon atomic lattice (dash line) and superlattice (solid line) with the tilting angle of θ=30°. Images are captured by the author.

3.2. Imaging Single Atom/Molecule

The adsorption of two-dimension (2D) nanostructures and molecules on clean surfaces are an interesting subject to determine their properties for catalysis, electronics, and corrosion applications. In early studies, the STM performed to determine the atomic resolution of surface or single-molecule images on surfaces. The diffusion, nucleation and growth mechanism of the chemisorbed or physisorbed molecules can be studied by STM at a variety temperature. Moreover, the STM can provide detailed information about the physical properties and adsorbent-surface interactions of atom/molecules. These nanostructure and molecule properties are mostly studied on well-known metal and semiconductor surfaces to eliminate the unknown surface effects.

Adsorbents on metal surfaces are generally induce a change in the local density of state near the Fermi level and electronic adsorbate resonance far away from Fermi level [75]. One of these adsorbents is magnetic materials such as Co, Fe, and Ni that are indispensable ingredients for magnetic recording media, spin-valve, magnetoresistance sensor, and hard drive sensor technologies [76-80]. The magnetic properties of these ferromagnetic materials can be tailored with the surface interaction. In Figure 6(a), the STM topography shows pure Co nanoisland formations on the Cu(111) surface at room temperature. The faulted (F) and unfaulted (U) islands have 2D triangle formation in terms of Cu(111) surface directions. Following, to control the spin depended tunneling in the Co island in-situ hydrogen adsorption performed using spin-polarized STM and STS techniques. The STM atomic manipulation technique was applied to desorb hydrogen. So controlling the surface magnetic properties has a great impact on spintronic applications of magnetic materials. This study is a good example that Co island can be imaged while determining the

magnetic and electronic properties via Cr-coated W tip and electrochemically etched Ni tip. Besides, it can be used as an atomic manipulation tool to modify the island magnetic properties via desorption of hydrogen molecules [81].

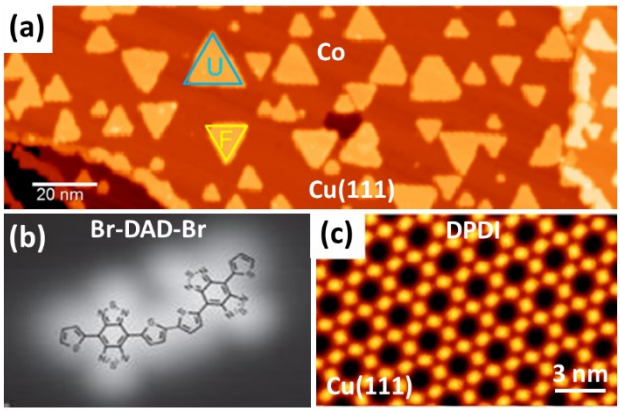

Figure 6: (a) STM topography of pure 2D Co nanoisland formations on Cu(111) surface shows unfaulted (U) and faulted (F) sites at room temperature [81]. (b) A selected structure of bis(5-bromo-2-thienyl)-benzobis(1,2,5-thiadiazole) molecule (Br-DAD-Br) image at 10 K [82] (c) STM image of 0.73 ML of DPDI molecule on Cu(111) surface after annealing the sample 473 K The image recorded at 77 K with a bias voltage of +2.5 V [83].

The charge transfer thought individual molecules are important for nanoelectronics applications [45]. Controlling chemical structure and electronic properties can be possible providing efficient charge transport, flexibility, and chemical stability for realistic applications. Therefore, the STM/S techniques are important to determine single-molecule chemical and electronic properties using the STM tip as an electron source and to study charge transfer thought the molecule. In Figure 6(b), the STM image shows one of selected structure of bis(5-bromo-2-thienyl)-benzobis(1,2,5-thiadiazole) molecule (Br-DAD-Br) at 10 K [82]. In this study, the electronic states (HOMO-LUMO) of different length DAD molecules measured by dI/dV spectroscopy. The STM is the most efficient method for molecular visualization among similar techniques. The STS produced a mapping of donor- and acceptor-like molecular states of DAD via applying a different bias voltage to clarify HOMO and LUMO states.

Metal-organic frameworks (MOFs) provide a functional ultrahigh surface area which is suitable for applications in catalysis, gas storage (hydrogen, methane), and chemical separation [84]. There has been a great deal of interest in investigating MOFs properties via STM [85]. The attractive force is primary interaction along with week van der Waals forces to form ordered MOF on metal surfaces. The STM image of the perylene derivative 4,9-diaminoperylene-quinone-3,10-diimine (DPDI) on the Cu(111) surface shows a unique hexagonal order along the surface after annealing the sample at 473 K [83]. The image in Figure 6(c) is recorded at 77 K. Well-ordered DPDI molecules exhibit 2D porous network due to attractive force and weak van der Waals force. Bias voltage-dependent imaging (from 2.5 to 3.4 V) provides a detailed molecular orientation of DPDI molecule on the Cu(111) surface.

Phosphorus (or boron) doped silicon technology reaching its limits, therefore, the scientist works on to find a new method to downscale the size of the transistor for device applications. One possible idea is to place individual atom and molecule on surfaces to build atomic-scale devices [86]. The STM atomic manipulation capability offers precise control of individual atom ejection via electron induces manipulation [87]. Figure 7(a) shows the design of the atomic-scale transistor on the Si(100) surface at room temperature. The STM was used in lithography mode to desorb hydrogen atoms in the desired area. Following, a Si adatom ejected via electron injection through the tip and replaced with PH3 in the middle of the image. The hydrogen-desorbed regions that are defined as source (S) and drain (D) and two gates (G1, G2) created by increased tunneling current [27]. This promising study reveals that single-atom devices can in principle be built about a few nm size transistors.

Recent investigations of well-ordered molecular structures on solid surfaces provide unique properties for molecular-based device applications [88, 89]. These structures can be formed of either the same or different molecules in which van der Waals forces, covalent bonding, and hydrogen bonding are the main forces [28, 90, 91]. Here, the deposited surface plays an important role in molecular order due to its electronic and physical properties. Using a low-temperature STM/S techniques the growth, adsorption, and electronic properties of the well-ordered molecular structures were studied with an advance of in-situ preparation. Figure 7(b) illustrates the STM image that shows the formation of iron phthalocyanine (FePc) molecule on 2D anisotropic triangular graphene monolayers growth on a Ru(0001) surface at 4.5 K [92]. The STM/S can reveal the selective adsorption of FePc molecules. More importantly, the STM is used as the lateral electric field source that can modify the molecular sites and orientations. This field creates well-ordered molecular structures due to a unique two-dimensional template of graphene.

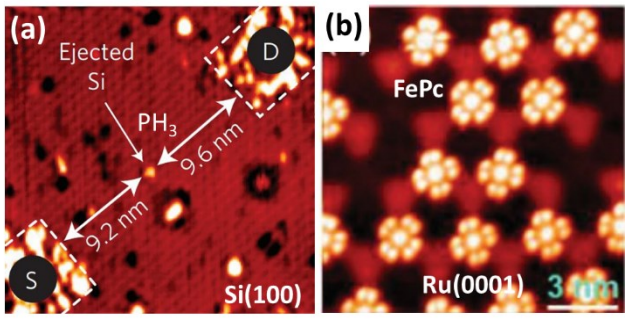

Figure 7: (a) The design of atomic-scale transistor on Si(100) surface at room temperature via ejecting Si adatom and replacing with PH_3 molecule, here source (S) and drain (D) regions are hydrogen desorbed regions via tip induced electron irritation [27]. (b) The STM topography iron phthalocyanine (FePc) molecule on 2D anisotropic triangular graphene monolayers on a Ru(0001) surface at 4.5 K [92].

STM measures the electric current between tip and the specimen ; the current was called tunnelling current; therefore, the technique was called as scanning tunnelling microscopy. The probe of the microscope was moved back and forth over the investigated specimen and current was obtained from specific points. The measured data was evaluated by the computer system and the image was obtained from investigated region. STM is one of the simplest techniques but it has some drawbacks. For example, it cannot be used in aqueous media and investigated sample should be conductive since the current between the tip and sample was measured to obtain an image. The tip moves up and down while moving on the surface to keep the current stable where the piezo actuators help them to make such a move. The data obtained from piezo actuators and the currents obtained from the tip was also used to improve the image obtained from the measurement.

3.3. Imaging Three-dimension Structures

The fundamental properties of two- and three-dimensions nanostructures can be determined by real-space imaging techniques that reveal the correlation between size, geometry, structure, and stability of clusters on surfaces [93]. These nanostructures are usually formed of metal clusters, molecular formations, and metal-molecule structures and exist together by covalent, chemical bonding or van der Waals force. Along with the achievement in the high-resolution image and spectroscopic capability of the STM, it can provide further information about matters at variety temperatures (liquid-He or -N_2, room, or high temperature up to 1000 K) at the nanoscale. The lateral size of the nanoparticles can be overestimated due to unavoidable convolution of the STM tip but there is no other method that can obtain single-particle (or molecule) images, local electronic and photonic properties [94].

Especially 3D metal nanoclusters promise potential applications in catalysis, quantum dot, biosensing, or drug delivery [95]. These clusters generally contain a few to thousands of atoms in one structure and can be synthesized *in-situ* or *ex-situ* by physical and chemical methods [96-100]. The characterization of these nanoclusters is based on the STM and STS techniques that provide high-reliability results via a single-electron transport of a single nanocluster [94]. Chemically synthesized Au_{374} cluster imaged under UHV condition using STM as seen in **Hata! Başvuru kaynağı bulunamadı.**(a). The STM determines the size and shape of clusters (indicated with blue dashed circles) and the red (1) and black (2) lines demonstrated the height profile of the clusters (about 3 nm) that are given inset plot in **Hata! Başvuru kaynağı bulunamadı.**(a). So the physical properties of the clusters are precisely determined at liquid-He temperature. Moreover, the STS measurements reveal the electronic properties of the clusters such as the highest occupied molecular orbital (HOMO) and lowest unoccupied molecular orbital (LUMO).

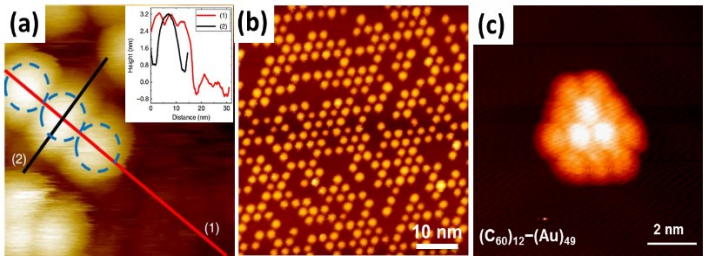

Figure 8: (a) STM topography of Ag_{374} clusters on Au(111) surface at LHe temperature. Inset plot: red (1) and black (2) height profile of Ag_{374} clusters (blue dashed circles) shows the cluster height [93] (http://creativecommons.org/licenses/by/4.0/.). (b) Monodisperse Ir clusters on graphene layer on Ir(111) surface with coverage of 0.003 ML [101] (c) Magic number $(C_{60})_{12}$-$(Au)_{49}$ hybrid cluster image on the Au(111) surface at room temperature [6].

Fabrication of monodisperse three-dimension metal clusters on a large flat surface is quite important to decorate uniform distribution on surfaces for potential applications [102]. Therefore, the graphene surface is widely used as a large flat substrate to growth monodisperse clusters to determine their chemical and physical properties [103-106]. Unlike oxide surfaces, the graphene surface provides more stability for metal clusters due to the high diffusion barrier and disallowing agglomeration. So, it allows us to determine single cluster properties without causing surface-related oxidation. Different systems have been studied using the STM for metal-graphene-metal interface applications such as Rh, Pt, W, Re, Fe, and Au clusters [107, 108]. **Hata! Başvuru kaynağı bulunamadı.**(b) shows one of the examples of the metal-graphene-metal systems which is the Ir cluster on the graphene surface with a coverage of 0.03 ML [101]. The STM image can reveal the monodisperse distribution of the clusters without agglomeration and the temperature-dependent study of STM showed that the clusters are stable up to a temperature of 600 K. So the temperature-dependent experiments are rather important for practical applications.

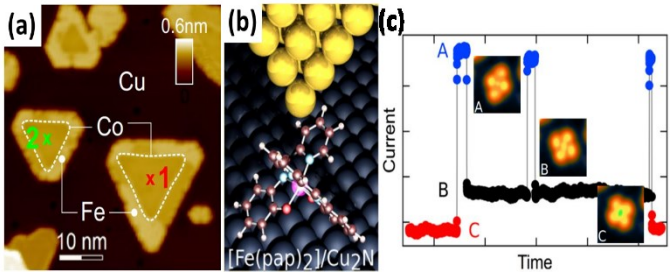

Figure 9: (a) STM image of triangular Co cores of Fe-decorated Co islands on Cu(111) surface [109] (http://creativecommons.org/licenses/by/4.0/). (b) Schematic diagram of an STM tip and $[Fe(pap)_2]^+$ molecule on $Cu_2N/Cu(100)$ surface [110]. (c) Three different states, A, B, and C, of Fe^{III} in molecule observed with different contrast and geometry (inset STM images) via recording the tunneling current as a function of time [110].

Three-dimension hybrid clusters also provide more interesting features of matters on surfaces. To obtain direct information about the self-assembly of supramolecular structures, the STM reveals high-resolution images down to a single intramolecular covalent bond. The hydrogen bonding and metal-ligand coordination hold together these supramolecular structures on the surface and the van der Waals interaction usually valid among the molecules [111]. One of these, the magic number C_{60}-Au hybrid cluster discovered by Xie et al. [111] on the Au(111) surface preparing sample *in-situ* STM chamber at 110 K and imaged at room temperature. These clusters $(C_{60})_m$-$(Au)_n$ exhibit certain number of m and n in the cluster with a unique geometry and stable up to 400 K. **Hata! Başvuru kaynağı bulunamadı.**(c) presents $(C_{60})_{12}$-$(Au)_{49}$ cluster in which Au island is surrounded by 9 C_{60} molecules and 3 on the top of it [6]. The bright feature of C_{60} molecules arises from a single atomic layer of Au island in the cluster. This feature determined by the height profile of the cluster. It is also claimed in this study that this process is a useful technique to fabricate magnetic quantum dot arrays for spin applications or single-molecule magnets via replacing the Au layer with magnetic atoms, such as Fe, Co, Ni, etc. [111]. The properties of magnetic nanostructures, such as ferromagnetism, antiferromagnetism, paramagnetism, can be determined by spin-polarized scanning tunneling microscopy and spectroscopy (SP-STM/S) [112, 113]. The SP-STM simply works based on a ferromagnetic nature tip (Fe, Co, Ni) or the tip edge covered with ferromagnetic material. Coil placed around the tip to control the directions of the tunneling electrons spins via inducing a magnetic field. These electrons carry charge and spin which is important for magnetically ordered materials to obtain local magnetic order of sample. The electron spins (up or down) define the material electron spins (up and down) due to the conversation of spin orientations [109]. The magnetization of the tip flips back and forth under the applied external field so the surface topography and magnetic contrast of the surface can be obtained separately. **Hata! Başvuru kaynağı bulunamadı.**(a) shows the STM image of triangular Fe-decorated Co cores on Cu(111) surface with using a Fe covered W tip. Providing STS data under applied external field reveals the local spin-polarization within a single nanostructure [109].

Understanding of molecular switching mechanism becomes a great interest for molecular spintronics applications in recent years [114]. This mechanism can be triggered either the molecule-substrate interaction or the STM tip manipulation which is usually based on tunneling current, electric field or mechanical contact. **Hata! Başvuru kaynağı bulunamadı.**(b) shows a schematic diagram of an STM tip and $[Fe(pap)_2]^+$ molecule for a molecular switching example. Using UHV-STM system, $[Fe(pap)_2]^+$ molecule successfully deposited on $Cu_2N/Cu(100)$ surface. It is observed that Fe^{III} provides three different states in the molecule [110]. The STM can detect these states with different contrast and geometry via recording tunneling current as a function of time. Continuous electron injection on the molecule results in a spin transition in the molecular state. As seen in **Hata! Başvuru kaynağı bulunamadı.**(c), these states represented as A, B, and C with high-resolution STM images (inset) seeing change in the tunneling current as a function of time.

References

1. Knoll, M., Ruska, E. , Das Elektronenmikroskop (Electron Microscopy) Z. Phys., 1932: p. 78318–339.
2. Hirsch, P.B., et al., Electron Microscopy of Thin Crystals. 1966: p. 20014.
3. Binnig, G., et al., Surface Studies by Scanning Tunneling Microscopy. Physical Review Letters, 1982. **49**(1): p. 57-61.
4. Eigler, D.M., Positioning Single Atoms with a Scanning Tunnelling Microscope. Nature, 1990. **344**: p. 524.
5. Kaya, D., et al., Controlled Manipulation of Magic Number Gold–Fullerene Clusters Using Scanning Tunneling Microscopy. Langmuir, 2018. **34**(28): p. 8388-8392.
6. Kaya, D., et al., Tip-triggered Thermal Cascade Manipulation of Magic Number Gold-fullerene Clusters in the Scanning Tunnelling Microscope. Nano Letters, 2017. **17**(10): p. 6171-6176.
7. Dmitry, A.O., et al., The Manipulation of C_{60} in Molecular Arrays with an STM Tip in Regimes Below the Decomposition Threshold. Nanotechnology, 2013. **24**(5): p. 055302.

8. Stróżecka, A., J. Mysliveček, and B. Voigtländer, Scanning Tunneling Spectroscopy and Manipulation of C_{60} on Cu(111). Applied Physics A, 2007. **87**(3): p. 475-478.

9. Hla, S.W., Scanning Tunneling Microscopy Single Atom/Molecule Manipulation and its Application to Nanoscience and Technology. Journal of Vacuum Science & Technology B, 2005. **23**(4): p. 1351-1360.

10. Stroscio, J.A. and R.J. Celotta, Controlling the Dynamics of a Single Atom in Lateral Atom Manipulation. Science, 2004. **306**(5694): p. 242-247.

11. Moriarty, P., et al., Translation, Rotation and Removal of C_{60} on Si(100)-2×1 Using Anisotropic Molecular Manipulation. Surface Science, 1998. **407**(1–3): p. 27-35.

12. Dujardin, G., et al., Vertical Manipulation of Individual Atoms by a Direct STM Tip-Surface Contact on Ge(111). Physical Review Letters, 1998. **80**(14): p. 3085-3088.

13. Beton, P.H., A.W. Dunn, and P. Moriarty, Manipulation of C_{60} Molecules on a Si surface. Applied Physics Letters, 1995. **67**(8): p. 1075-1077.

14. Kaya, D., The effect of electric field on a fullerene molecule on a metal surface by a nano STM tip. Physica B-Condensed Matter, 2019. **557**: p. 126-131.

15. Niu, T., Electric-Field-Induced Molecular Switch of Single Dipolar Phthalocyanine on Cu(111): A Scanning Tunneling Microscopy Study. The Journal of Physical Chemistry C, 2015. **119**(34): p. 19802-19807.

16. Alemani, M., et al., Electric Field-Induced Isomerization of Azobenzene by STM. Journal of the American Chemical Society, 2006. **128**(45): p. 14446-14447.

17. Stokbro, K., U. Quaade, and F. Grey, Electric Field Effects in Scanning Tunneling Microscope Imaging. Applied Physics A, 1998. **66**(1): p. S907-S910.

18. Tsong, T.T., Effects of an Electric Field in Atomic Manipulations. Physical Review B, 1991. **44**(24): p. 13703-13710.

19. Dujardin, G., et al., DIET at the Nanoscale. Surface Science, 2016. **643**: p. 13-17.

20. Wykrota, A., et al., A Molecular Switch Based on the Manipulation of 1,3-dichlorobenzene on Ge(001) Between Two Adsorption Sites by Inelastic Tunneling Electrons. Physical Chemistry Chemical Physics, 2015. **17**(43): p. 28830-28836.

21. Hla, S.W. and K.H. Rieder, STM Control of Chemical Reaction: Single-Molecule Synthesis. Annual Review of Physical Chemistry, 2003. **54**: p. 307-330.

22. Gross, L., et al., Bond-Order Discrimination by Atomic Force Microscopy. Science, 2012. **337**(6100): p. 1326-1329.

23. Gross, L., et al., High-Resolution Molecular Orbital Imaging Using a p-Wave STM Tip. Physical Review Letters, 2011. **107**(8): p. 086101.

24. Gross, L., et al., The Chemical Structure of a Molecule Resolved by Atomic Force Microscopy. Science, 2009. **325**(5944): p. 1110-1114.

25. Chen, C.J., Introduction to Scanning Tunneling Microscopy. 2007, New York: Oxford University Press.

26. McNab, I.R. and J.C. Polanyi, Patterned Atomic Reaction at Surfaces. Chemical Reviews, 2006. **106**(10): p. 4321-4354.

27. Fuechsle, M., et al., A single-atom transistor. Nature Nanotechnology, 2012. **7**: p. 242.

28. Gao, J., et al., Probing Phase Evolutions of Au-Methyl-Propyl-Thiolate Self-Assembled Monolayers on Au(111) at the Molecular Level. The Journal of Physical Chemistry B, 2018.

29. Guan, B., et al., Nanoscale Nitrogen Doping in Silicon by Self-Assembled Monolayers. Scientific Reports, 2015. **5**: p. 12641.

30. Burgi, T., Properties of the gold-sulphur interface: from self-assembled monolayers to clusters. Nanoscale, 2015. **7**(38): p. 15553-15567.

31. Shen, C. and M. Buck, Nanoscale Patterning of a Self-assembled Monolayer by Modification of the Molecule–substrate Bond. Beilstein Journal of Nanotechnology, 2014. **5**: p. 258-267.

32. Li, Y. and N. Lin, Combined Scanning Tunneling Microscopy and Kinetic Monte Carlo Study on Kinetics of Cu-coordinated Pyridyl-porphyrin Supramolecular Self-assembly on a Au(111) Surface. Physical Review B, 2011. **84**(12): p. 125418.

33. Chakrabarty, R., P.S. Mukherjee, and P.J. Stang, Supramolecular Coordination: Self-Assembly of Finite Two- and Three-Dimensional Ensembles. Chemical Reviews, 2011. **111**(11): p. 6810-6918.

34. Heim, D., et al., Surface-Assisted Assembly of Discrete Porphyrin-Based Cyclic Supramolecules. Nano Letters, 2010. **10**(1): p. 122-128.

35. Sánchez, L., et al., Ordering Fullerenes at the Nanometer Scale on Solid Surfaces. Chemical Reviews, 2009. **109**(5): p. 2081-2091.

36. Joachim, C., J.K. Gimzewski, and A. Aviram, Electronics Using Hybrid-molecular and Mono-molecular Devices. Nature, 2000. **408**(6812): p. 541-548.

37. Liu, L., et al., Switching Molecular Orientation of Individual Fullerene at Room Temperature. Scientific Reports, 2013. **3**: p. 3062.

38. Gruznev, D.V., et al., Stepwise Self-assembly of C_{60} Mediated by Atomic Scale Moiré Magnifiers. Nature Communication, 2013. **4**: p. 1679.

39. Chen, W., et al., Orientationally Ordered C_{60} on p-Sexiphenyl Nanostripes on Ag(111). ACS Nano, 2008. **2**(4): p. 693-698.

40. Martsinovich, N. and L. Kantorovich, Theoretical Modelling of Tip Effects in the Pushing Manipulation of C_{60} on the Si(001) Surface. Nanotechnology, 2008. **19**(23): p. 235702.

41. Tang, H., et al., Fundamental Considerations in the Manipulation of a Single C_{60} Molecule on a Surface with an STM. Surface Science, 1997. **386**(1–3): p. 115-123.

42. Cuberes, M.T., R.R. Schlittler, and J.K. Gimzewski, Room Temperature Repositioning of Individual C_{60} Molecules at Cu Steps: Operation of a Molecular Counting Device. Applied Physics Letters, 1996. **69**(20): p. 3016-3018.

43. Stroscio, J.A., R.M. Feenstra, and A.P. Fein, Electronic Structure of the Si(111)2x1 Surface by Scanning-Tunneling Microscopy. Physical Review Letters, 1986. **57**(20): p. 2579-2582.

44. Young, R., J. Ward, and F. Scire, Observation of Metal-Vacuum-Metal Tunneling, Field Emission, and the Transition Region. Physical Review Letters, 1971. **27**(14): p. 922-924.

45. Joachim, C. and M.A. Ratner, Molecular Electronics: Some Views on Transport Junctions and Beyond. PNAS, 2005. **102**(25): p. 8801-8808.

46. Binnig, G. and D.P.E. Smith, Single-tube three-dimensional scanner for scanning tunneling microscopy. Review of Scientific Instruments, 1986. **57**(8): p. 1688-1689.

47. Frohn, J., et al., Coarse tip distance adjustment and positioner for a scanning tunneling microscope. Review of Scientific Instruments, 1989. **60**(6): p. 1200-1201.

48. Huey, D.A.B.B.D., Scanning Probe Microscopy and Spectroscopy: Theory, Techniques, and Applications. 2nd ed. 2001, New York: Wiley-VCH.

49. Mould, R., Pierre Curie, 1859–1906. Current oncology, 2007. **14**(2): p. 74.

50. Curie, J. and P. Curie, Développement par compression de l'électricité polaire dans les cristaux hémièdres à faces inclinées. Bulletin de minéralogie, 1880. **3**(4): p. 90-93.

51. Karle, J.t. and I. Karle, The symbolic addition procedure for phase determination for centrosymmetric and non-centrosymmetric crystals. Acta Crystallographica, 1966. **21**(6): p. 849-859.

52. Zhang, J., et al., Large field-induced strains in a lead-free piezoelectric material. Nature Nanotechnology, 2011. **6**(2): p. 98.

53. Ren, B., G. Picardi, and B. Pettinger, Preparation of Gold Tips Suitable for Tip-enhanced Raman Spectroscopy and Light Emission by Electrochemical Etching. Review of Scientific Instruments, 2004. **75**(4): p. 837-841.

54. Rogers, B.L., et al., A Method for Production of Cheap, Reliable Pt–Ir Tips. Review of Scientific Instruments, 2000. **71**(4): p. 1702-1705.

55. Khan, Y., et al., Two-step Controllable Electrochemical Etching of Tungsten Scanning Probe Microscopy Tips. Review of Scientific Instruments, 2012. **83**(6): p. 063708.

56. Lucier, A.-S., et al., Determination of the Atomic Structure of Scanning Probe Microscopy Tungsten tips by Field Ion Microscopy. Physical Review B, 2005. **72**(23): p. 235420.

57. Kim, P., et al., Efficient Electrochemical Etching Method to Fabricate Sharp Metallic tips for Scanning Probe Microscopes. Review of Scientific Instruments, 2006. **77**(10): p. 103705-103706.

58. Kar, A.K., et al., A Reverse Electrochemical Floating-layer Technique of SPM tip Preparation. Measurement Science and Technology, 2000. **11**(10): p. 1426.

59. Ekvall, I., et al., Preparation and Characterization of Electrochemically Etched W tips for STM. Measurement Science and Technology, 1999. **10**(1): p. 11.

60. Oliva, A.I., et al., Electrochemical Preparation of Tungsten Tips for a Scanning Tunneling Microscope. Review of Scientific Instruments, 1996. **67**(5): p. 1917-1921.

61. Hołyst, R. and M. Litniewski, Evaporation into Vacuum: Mass Flux from Momentum Flux and the Hertz–Knudsen Relation Revisited. The Journal of Chemical Physics, 2009. **130**(7): p. 074707.

62. Nevshupa, R.A. and L.S. Sinev, Model of Pressure Variation in a Vacuum System for Volatile Liquid Evacuation. Technical Physics. **50**(10): p. 1255-1258.

63. Instrumentation Reference Book, ed. W. Boyes. 2003, Agilend Technologies: Butterworth Heinemann.

64. Chikkamaranahalli, S.B., et al. Damping mechanisms for precision applications in UHV environment. in American Society for Precision Engineering. 2006. Citeseer.

65. Bai, C., Scanning Tunneling Microscopy and Its Application. 2 ed. Springer Series in Surface Sciences. 2000, Berlin: Springer-Verlag Berlin Heidelberg.

66. Besenbacher, F., et al., Atomic-scale Surface Science Phenomena Studied by Scanning Tunneling Microscopy. Surface Science, 2009. **603**(10–12): p. 1315-1327.

67. Hallmark, V.M., et al., Observation of Atomic Corrugation on Au(111) by Scanning Tunneling Microscopy. Physical Review Letters, 1987. **59**(25): p. 2879-2882.

68. Wöll, C., et al., Determination of Atom Positions at Stacking-fault Dislocations on Au(111) by Scanning Tunneling Microscopy, in Scanning Tunneling Microscopy, H. Neddermeyer, Editor. 1993, Springer Netherlands. p. 114-117.
69. Narasimhan, S. and D. Vanderbilt, Elastic Stress Domains and the Herringbone Reconstruction on Au(111). Physical Review Letters, 1992. **69**(10): p. 1564-1567.
70. Bürgi, L., H. Brune, and K. Kern, Imaging of Electron Potential Landscapes on Au(111). Physical Review Letters, 2002. **89**(17): p. 176801.
71. Marchini, S., S. Günther, and J. Wintterlin, Scanning tunneling microscopy of graphene on Ru (0001). Physical Review B, 2007. **76**(7): p. 075429.
72. Hsu, J.W.P., et al., Si(111)(7 x 7) Dangling Bond Contribution to Surface Recombination. Journal of Vacuum Science & Technology A 1992. **10**(4): p. 985-989.
73. Geim, A.K., Graphene prehistory. Physica Scripta, 2012. **T146**: p. 014003.
74. Morgenstern, M., Scanning tunneling microscopy and spectroscopy of graphene on insulating substrates. physica status solidi (b), 2011. **248**(11): p. 2423-2434.
75. Lang, N.D., Theory of Single-Atom Imaging in the Scanning Tunneling Microscope. Physical Review Letters, 1986. **56**(11): p. 1164-1167.
76. Jensen, P.J., Magnetic recording medium with improved temporal stability. Applied Physics Letters, 2001. **78**(15): p. 2190-2192.
77. Fujita, M., et al., Exchange coupling in spin-valve structures containing amorphous CoFeB. Journal of Applied Physics, 1997. **81**(8): p. 4909-4911.
78. Ross, C., Patterned Magnetic Recording Media. Annual Review of Materials Research, 2001. **31**(1): p. 203-235.
79. W. F. Egelhoff, J., et al., Growth of giant magnetoresistance spin valves using indium as a surfactant. Journal of Applied Physics, 1996. **79**(5): p. 2491-2496.
80. Kaya, D., et al., Controlling exchange bias in FeMn with Cu. Journal of Applied Physics, 2013. **113**(17): p. 17D717.
81. Park, J., et al., Surface Magnetism of Cobalt Nanoislands Controlled by Atomic Hydrogen. Nano Letters, 2017. **17**(1): p. 292-298.
82. Nacci, C., et al., Conductance of a single flexible molecular wire composed of alternating donor and acceptor units. Nature Communications, 2015. **6**: p. 7397.
83. Matena, M., et al., On-surface synthesis of a two-dimensional porous coordination network: Unraveling adsorbate interactions. Physical Review B, 2014. **90**(12): p. 125408.
84. Schröder, M., Functional metal-organic frameworks: gas storage, separation and catalysis. Vol. 293. 2010: Springer.
85. Ariga, K., et al., Nanoarchitectonics for Dynamic Functional Materials from Atomic-/Molecular-Level Manipulation to Macroscopic Action. Advanced Materials, 2016. **28**(6): p. 1251-1286.
86. Koenraad, P.M. and M.E. Flatté, Single dopants in semiconductors. Nature Materials, 2011. **10**: p. 91.
87. Inami, E., et al., Room-Temperature-Concerted Switch Made of a Binary Atom Cluster. Nature Communication, 2015. **6**.
88. Gao, H.J. and L. Gao, Scanning tunneling microscopy of functional nanostructures on solid surfaces: Manipulation, self-assembly, and applications. Progress in Surface Science, 2010. **85**(1): p. 28-91.
89. Barth, J.V., G. Costantini, and K. Kern, Engineering atomic and molecular nanostructures at surfaces, in Nanoscience and Technology. p. 67-75.
90. Guo, L.a., et al., Orientational Epitaxy of van der Waals Molecular Heterostructures. Nano Letters, 2018. **18**(8): p. 5257-5261.
91. Gao, J., et al., Growth of Two-Dimensional C60 Nanoclusters within a Propylthiolate Matrix. The Journal of Physical Chemistry C, 2016. **120**(44): p. 25481-25488.
92. Zhang, H.G., et al., Assembly of iron phthalocyanine and pentacene molecules on a graphene monolayer grown on Ru(0001). Physical Review B, 2011. **84**(24): p. 245436.
93. Zhou, Q., et al., Real-space imaging with pattern recognition of a ligand-protected Ag(374) nanocluster at sub-molecular resolution. Nature Communications, 2018. **9**(1): p. 2948-2948.
94. Kano, S., T. Tada, and Y. Majima, Nanoparticle characterization based on STM and STS. Chemical Society Reviews, 2015. **44**(4): p. 970-987.
95. Jena, P. and Q. Sun, Super Atomic Clusters: Design Rules and Potential for Building Blocks of Materials. Chemical Reviews, 2018. **118**(11): p. 5755-5870.
96. Yulikov, M., et al., Binding of Single Gold Atoms on Thin MgO(001) Films. Physical Review Letters, 2006. **96**(14): p. 146804.
97. Repp, J., et al., Controlling the Charge State of Individual Gold Adatoms. Science, 2004. **305**(5683): p. 493-495.
98. Olsson, F.E., et al., Multiple Charge States of Ag Atoms on Ultrathin NaCl Films. Physical Review Letters, 2007. **98**(17): p. 176803.
99. Fu, Q., et al., Interface-Confined Ferrous Centers for Catalytic Oxidation. Science, 2010. **328**(5982): p. 1141-1144.
100. Schouteden, K., et al., Probing the atomic structure of metallic nanoclusters with the tip of a scanning tunneling microscope. Nanoscale, 2014. **6**(4): p. 2170-2176.

101. N'Diaye, A.T., et al., Two-Dimensional Ir Cluster Lattice on a Graphene Moire on Ir(111). Physical Review Letters, 2006. **97**(21): p. 215501.
102. Meiwes-Broer, K.-H., Metal clusters at surfaces: structure, quantum properties, physical chemistry. 2012: Springer Science & Business Media.
103. Gao, M., et al., Tunable interfacial properties of epitaxial graphene on metal substrates. Applied Physics Letters, 2010. **96**(5): p. 053109.
104. Gao, L., J.R. Guest, and N.P. Guisinger, Epitaxial Graphene on Cu(111). Nano Letters, 2010. **10**(9): p. 3512-3516.
105. Wofford, J.M., et al., Extraordinary epitaxial alignment of graphene islands on Au(111). New Journal of Physics, 2012. **14**(5): p. 053008.
106. Liang, Z., et al., Graphene domain boundaries on Pt(111) as nucleation sites for Pt nanocluster formation. Surface Science, 2012. **606**(21): p. 1643-1648.
107. Cavallin, A., et al., Local Electronic Structure and Density of Edge and Facet Atoms at Rh Nanoclusters Self-Assembled on a Graphene Template. ACS Nano, 2012. **6**(4): p. 3034-3043.
108. N'Diaye, A.T., et al., A versatile fabrication method for cluster superlattices. New Journal of Physics, 2009. **11**(10): p. 103045.
109. Phark, S.-h. and D. Sander, Spin-polarized scanning tunneling microscopy with quantitative insights into magnetic probes. Nano Convergence, 2017. **4**(1): p. 8.
110. Jasper-Toennies, T., et al., Robust and Selective Switching of an FeIII Spin-Crossover Compound on Cu2N/Cu(100) with Memristance Behavior. Nano Letters, 2017. **17**(11): p. 6613-6619.
111. Xie, Y.-C., L. Tang, and Q. Guo, Cooperative Assembly of Magic Number C_{60}-Au Complexes. Physical Review Letters, 2013. **111**(18): p. 186101.
112. Oka, H., et al., Spin-polarized quantum confinement in nanostructures: Scanning tunneling microscopy. Reviews of Modern Physics, 2014. **86**(4): p. 1127-1168.
113. Wulfhekel, W. and J. Kirschner, Spin-Polarized Scanning Tunneling Microscopy of Magnetic Structures and Antiferromagnetic Thin Films. Annual Review of Materials Research, 2007. **37**(1): p. 69-91.
114. Dediu, V.A., et al., Spin routes in organic semiconductors. Nature Materials, 2009. **8**: p. 707.